

# Vibrational and fluorescence spectroscopy mapping structural rearrangement in edible *Samia ricini* (Eri) pupae proteins during ultrasound assisted extraction and their in-depth proteome profiling

**Preeti Sarkar**

Tezpur University

**Nemnunhoi Haokip**

Tezpur University

**Charu Lata Mahanta**

Tezpur University

**Raj Kumar Duary** (✉ [rkduary@bhu.ac.in](mailto:rkduary@bhu.ac.in))

Banaras Hindu University

---

## Research Article

**Keywords:** Proteomics, structural analysis, particle size, fluorescence, spectroscopy, edible pupae proteins

**Posted Date:** April 14th, 2022

**DOI:** <https://doi.org/10.21203/rs.3.rs-1536968/v1>

**License:**  This work is licensed under a Creative Commons Attribution 4.0 International License. [Read Full License](#)

---

## Abstract

The present study initially investigated the optimum conditions for maximum protein separation from edible Eri pupae using 150-400W ultrasound power within 5–30 min having a protein yield of > 50% for establishing any significant conformational and physico-chemical alterations. Results showed that 5 min of ultrasonic treatment was feasible to improve extraction yield with increasing power value, best of 250-300W with 20 min treatment. Ultrasound assisted extracted protein at 67.5, 71.4 and 76.4 J mL<sup>-1</sup> exhibited maximum secondary structural changes with an increase in varied disorganized structures. The temperature factor was more evident above 75°C, causing significant shifts in a Fourier transform infrared (FTIR) region of 1620–1642 cm<sup>-1</sup>, particularly with a deviation of intermolecular  $\beta$ -sheets. The Raman band intensity pattern at 2929 and 1440–1465 cm<sup>-1</sup> was highest in sonicated treatment at 67.5 J mL<sup>-1</sup> and then significantly declined. Thus, indicating cross-linkage due to the formation of new unstable intermolecular S-S bond in samples treated at 71.4 and 76.4 J mL<sup>-1</sup>, which explains the polarity of the microenvironment nearby hydrogen bonds, consistent with particle size and thermal characterization data. The peaks at 2014, 2168, and 2420 cm<sup>-1</sup> gradually disappeared with increased in ultrasonic energy input, probably depicting the development of firm 3-D network-like structures. Around 107 distinct proteins in Eri pupae assigned to 26 insect protein families were deduced via MS/MS investigation of pellet and supernatant. The outcomes will later facilitate in identifying the protein-protein interrelations accountable for functional aspects of product developed with Eri pupae protein isolate.

## 1. Introduction

Insects are alluring increasing attention in respect of their advantages in sustainable agriculture, prospects to assist in demanding nutritional requirements as an alternative protein source (50–82%, dry weight), or utilizing these proteins for the invention of innovative biomaterials (Bao, et al., 2020; Zhao et al., 2016; Zielinska et al., 2015). Modifying molecular structure on the micro and macroscales can escort the composition of functional components, thus establishing the correlation between protein structure and functionality. Acceptance of insects, particularly in everyday food habits is not feasible due to their visible and intangible characteristics. So, to enhance their acceptance, the functional properties of proteins and lipids extracted from insects (such as larvae and pupae of mealworm and silkworm, crickets, caterpillar, etc.) for development of insect-based food products or incorporation in additional foods have been recently assessed in diverse studies. For example, protein powders from edible insects have been investigated as constituents for the preparation of sausages, tortillas, dairy products, and biscuits with interest in their application as a texturizing ingredient by following their functional properties (Akande et al., 2020; David Birman et al., 2021; Kim et al., 2016; Luna et al., 2021). In the sericulture industry, plenty of unwanted byproducts like sericin and silkworm pupae are produced to a great extent each year; this imparts possibilities to employ such low-cost supplies to innovate novel value-added products. Mulberry silkworm (*Bombyx mori*) pupae have been extensively explored and implemented for product development. Nevertheless, reports on the native non-mulberry silkworm species (*Samia ricini*) as functional protein or nutraceutical ingredients are still lacking. This silkworm is locally known as "Eri silk", and a substantial mass of unused pupae piled up in local reeling industries in particular regions of North Eastern states in India. These are either discarded or traditionally incorporated by the native groups as a delicacy in fermented or cooked form for a very long time (Mishra et al., 2003).

Chemical methods utilizing NaOH or HCL have been chiefly reported for insect protein extraction through an iso-precipitation method, which is relatively time-consuming, expensive, and includes reasonable loss of solvent (Zhou et al., 2017; Zielinska et al., 2015). For the last two decades, ultrasound with a power scale wavering between 10-1000 W/cm<sup>2</sup> and 16–100 kHz of frequency reported significant improvement in the extraction rate of bioactive compounds (such as starch, proteins, flavones, polyphenols, lipids, etc.) (Kadam et al., 2015; Shirsath et al., 2012). For insects, significantly less is known concerning the impact of altering the conditions of ultrasound treatment on the extraction of their proteins. The primary mechanism behind ultrasound effects in enhancing extraction yield is related to cyclic generation and rapid collapse of asymmetric microbubble, heating, dynamic agitation, shear stresses, and turbulence resulting in mass transfer phenomenon in the locality of cavitation zones (Preece et al., 2017). However, some studies have widely reported that sonication-induced shear forces, turbulence, and heat generated in the cavitation medium can affect proteins' physicochemical and structural state, directly contributing to end-product value and quality. During ultrasound processing, proteins encounter a sequence of changes because of rearrangement in secondary conformation; certain molecular regions like free SH-groups or hydrophobic zones become available to new inter or intramolecular associations, developing aggregates through non-covalent and covalent crosslinks. Therefore, resulting in manipulations in textural characteristics and functional attributes accompanied by modification in end-product quality (Kang et al., 2021; Tellez-Morales et al., 2020). Thus, regulating ultrasonic parameters such as frequency, amplitude, and processing time that mainly influence cavitation intensity needs analysis for maximum targeted product yield and the identification of changes that could assist in improving the conditions leading to better-quality product outcomes.

Given Eri pupae's importance with high protein bioavailability and essential amino acids, as reported by Longwah et al. (2011), its value enhances by applying ultrasound to increase protein extraction. Thus, the primary aim of this study was to investigate and compare the effects of sonication on the maximum extraction yield and molecular structure of Eri pupae proteins with conventional alkaline extraction as a function of the ultrasound power (150–400 W) and time (5–30 min) of treatment. It will help us to derive an interpretation of the physicochemical effects of ultrasound on pupae proteins, which may contribute to its functional applications. Therefore, in this study, we extended our investigations by combining both vibrational and fluorescence spectroscopy to fingerprint major selected mechanisms underlying the evolution of any conformational changes of pupae proteins during ultrasound-assisted extraction conditions. We believe that Eri pupae consist of a complex protein system. So, our next aim was to carry out proteome profiling of extracted Eri pupae proteins for the first time. Such information could later assist in predicting the type of protein-protein interactions responsible for the product's functional characteristics developed with Eri pupae protein isolate.

## 2. Materials And Methods

### 2.1. Materials and reagents

*Samia ricini* pupae were collected from the local commercial market and the sericulture farms of Karbianglong and Sonitpur district, Assam, India, respectively. Pupae with no apparent injuries and infections were selected, maintained at 23–25 °C, and transferred to the lab at the earliest. The taxonomic recognition was further established by the Zoological Society of India, Kolkata. Collected pupae were physically cleaned and then kept at -20 °C till the subsequent use. Pupae were minced before freeze-drying and then ground ( $\leq 20$  °C) into powder. Using n-hexane (1:5, w/v), the procured powder was defatted twice for 6 h in a Soxhlet apparatus accompanied by drying in a hot air oven at 50 °C. All other reagents, solvents, and chemicals utilized were of analytical grade if not explicitly mentioned.

## 2.2. Sonication treatment

Firstly, for ultrasonic-assisted extraction (UAE), the mixtures (defatted pupae powder in water, 10% w/v) were adjusted to attain a pH of 9.5 by adding 3 M sodium carbonate. The suspensions were placed in an ice bath after continuously stirring (at 200 rpm) for 2 h at room temperature (28–35 °C) and then sonicated (using a probe sonicator of 20 kHz and 13 mm diameter, U500, Takashi Japan) at different power levels output of 150, 200, 250, 300, 350 and 400W for 0, 5, 10, 15, 20, 25 and 30 min (ON/OFF time 5/1 s). Initial and final temperatures were recorded to determine the power dissipated in the solution and calculate specific energy. Afterward, the slurry of each treatment was cooled down and then immediately centrifuged (8000 x g, 4 °C, and 15 min). The pellets obtained were weighed and freeze-dried, whereas the pH of the collected supernatant was brought to 4.3 using 3 M citric acid and centrifuged again (same condition). The precipitates collected were washed twice; pH was brought to 7.0 before lyophilization and named "Eri pupae protein isolate (EPPI)". The protein isolate obtained using an alkaline extraction procedure without ultrasound treatment was considered a control. Samples were subjected to the micro-Kjeldahl method and examined for protein concentration. The protein yield in each sample (Eq. 1) was calculated as follows:

$$Protein\ extraction\ yield(\%) = [(S. x_{p,s}) / (S. x_{p,s} + P. x_{p,p})] \times 100$$

1

where, S and P represent the total weight of supernatant precipitates and pellet, respectively,  $x_{p,s}$  and  $x_{p,p}$  denotes the mass fraction of protein available in supernatant and pellet, respectively.

The actual ultrasonic power ( $P_a$ ) utilized during each sonication process was calculated applying Eq. (2) (Gonzalez-Centeno et al., 2014).

$$P_a = m. c_p \left( \frac{\Delta T}{\Delta t} \right)$$

2

where,  $P_a$  denotes acoustic power (W),  $m$  denotes the total mass of sample (g),  $c_p$  denotes specific heat capacity (4181 J kg<sup>-1</sup> K<sup>-1</sup>),  $\Delta t$  and  $\Delta T$  denote time and temperature variance, respectively.

Specific energy absorbed by each sample mixture was quantified by Eq. (3) (Strieder et al., 2019).

$$Specific\ energy\ (JmL^{-1}) = \frac{P_a \times t}{V \times TS}$$

3

where,  $P_a$  denotes acoustic power (W),  $t$  denotes time (s),  $TS$  denotes the total solid of defatted pupae powder (g), and  $V$  denote the volume of slurry (mL).

## 2.3. Protein solubility

The protein solubility was evaluated by calculating the protein concentration (Eq. 4) in the supernatants by the Lowry method using BSA as standard at 750 nm.

$$Protein\ solubility(\%) = 100 \times \frac{Protein\ content\ of\ the\ supernatant}{Total\ protein\ content}$$

4

## 2.4. Confocal laser microscopy

The impact of ultrasound treatment on Eri pupae slurries (5%, w/v) was visualized through confocal laser scanning microscopy (TCS SP8, Leica, Germany) using rhodamine B (7% w/v, Sigma-Aldrich, USA). Scanning was acquired at an excitation wavelength of 560 nm and an emission wavelength of 626 nm.

## 2.5. Determination of particle size distribution

The particle sizes in pupae slurries obtained after ultrasound treatment were recorded through a particle size analyzer (Mastersizer 2000, Malvern Instruments, UK). The disperse phase was assigned to a refractive index of 1.32 and 1.47. Particle size distribution was identified by D[3,2] and D[4,3]. Moreover, for small particles (< 1  $\mu$ m)  $d[3,2]$  and  $d[4,3]$  were calculated. The span value (Eq. 5) calculated to analyze the size distribution in a sample was as follows:

$$Span / Polydispersity\ index = \frac{Dv(0.9) - Dv(0.1)}{Dv(0.5)}$$

Where,  $D_v(0.9)$ ,  $D_v(0.1)$ , and  $D_v(0.5)$  denotes correspondent volume diameters at 90, 10 and 50% collective volume, respectively. The particle sizes and span values were established as the mean and standard deviation of fifteen readings recorded for each sample with triplicates.

## 2.5. Determination of thermal characteristics

Ultrasound extracted proteins were determined for their thermal properties using a digital scanning calorimeter (Netzsch, Germany) according to the procedure reported by Feyzi et al. (2018). 12 mg of EPPI placed in an aluminum pan was scanned at  $10^\circ\text{C min}^{-1}$  within a scale of  $10\text{--}150^\circ\text{C}$ . Employing Universal Analysis V4.2E (New Castle, USA), thermal parameters such as denaturation enthalpy variation ( $\Delta H_d$ ), denaturation temperature ( $T_d$ ), and onset denaturation temperature ( $T_o$ ) were calculated.

## 2.6. Fourier transform infrared spectroscopy (FTIR)

FTIR spectrum of 0.5 g of the treated sample was obtained (FTIR spectrometer, Frontier, PerkinElmer, Boston, MA, USA) in the  $4000\text{--}600\text{ cm}^{-1}$  range. The final spectrum was procured as the mean of 25 scans recorded for each sample at a resolution of  $2\text{ cm}^{-1}$ . The collected spectra were exported and refined for baseline correction, subtraction of water spectra, and then normalized employing Unscrambler software (Version 10.2, CAMO AS, Trondheim, Norway) for further analysis. This work focused on investigating alterations in the secondary conformation of proteins yielded by ultrasound-assisted extraction. Principal component analysis (PCA) was applied solely on the amide I ( $1700\text{--}1600\text{ cm}^{-1}$ ) regions of the spectra for quantitative scanning by implementing a non-linear curve fitting, analyzing if the changes were significantly sufficient to categorize sonication treated samples into different groups. Briefly, the bands obtained from amide I region spectra were distinguished and isolated using the Gaussian function (Origin 8.0, Origin Lab Corp, USA) after their derivatization (polynomial order 2, 11-point smoothing), smoothing, and normalization. During the curve fitting process, the parameters (such as position, height, bandwidth, and baseline) for each condition that might fit the original spectrum in the best way were optimized through Gaussian-shaped curves and chi-square values. In our work, the chi-square values and residuals plots obtained after the typical peak fit were  $\sim 1.5 \times 10^{-6}$  and showed  $\pm 0.006$  values, respectively, indicating a good fit. Later, the band area for individual wavelength allotted to a particular secondary conformation was calculated to determine the comparative subscription of each component after the fit was considered acceptable.

## 2.7. Raman spectroscopy

Raman spectra ( $3000\text{--}400\text{ cm}^{-1}$ ) of 0.5 g samples were obtained from a Vecta-plus interferometer stationed in the FT-Raman spectrometer (Renishaw basis series, Renishaw, UK) as the mean of 25 scans recorded for each sample at a resolution of  $4\text{ cm}^{-1}$ , excitation at 630.5 nm and power at 7 mW. Processing and analysis of spectra were performed using WIRE 3.4 along with the similar method described for FTIR spectroscopy.

## 2.8. Fluorescence spectroscopy of ultrasound extracted proteins

The fluorescence spectrum was recorded using a fluorescence spectrophotometer (Cary Eclipse, Agilent Technologies, Santa Clara, USA) connected with a 150W Xenon lamp. To measure tryptophan fluorescence ( $F_{trp}$ ), excitation at 290 nm was allowed with emission at 300–450 nm. An excitation wavelength of 315 nm was used for dityrosine fluorescence ( $F_{dt}$ ), with emission recorded at 380–480 nm. All scans were carried out in triplicate for each sample.

## 2.9. Molecular mass analyses of Eri pupae proteins

The molecular weight of the proteins (400  $\mu\text{g}$ ) available in supernatant and pellet fractions was studied by 12.5% SDS-PAGE at reduced and non-reduced conditions. The gels were first stained with 0.1% Coomassie Brilliant Blue R-250 and later washed in a destaining solution made of water, methanol, and acetic acid at a 50:40:10 ratio to investigate respective bands. Band intensities were analyzed using ImageJ software. Molecular masses of proteins in supernatant and pellet fractions were additionally acclaimed by employing UltrafleXtreme MALDI TOF/TOF™ Analyzer, Bruker Daltonik, according to our earlier procedure (Sarkar et al., 2021).

## 3.0. Lc-ms/ms Analysis Of Trypsin Digested Gel

Based on our previous method (Sarkar et al., 2021), raw LC-MS/MS data (Nano-UHPLC (Agilent 1260) equipped with Q-TOF mass spectrometer (Agilent 6530)) were prepared by employing the Mascot search engine (version 2.3) after individually probing against the UniProt database non-redundant entries of insecta (taxid: 50557; protein entries: 5173744), *Samia* (taxid: 7126; protein entries: 687) and *Samia ricini* (taxid: 63990; protein entries: 376) from 4 and 2 gel fractions of supernatant and pellet, respectively. The average relative existence of the Eri pupae proteome was determined by MS1 (Summed peptide spectral intensity of matched precursor) and MS2 (Mean spectral intensity).

## 3.1. Statistical analysis

Experiments were repeated at least three times (if not mentioned before), and results were analyzed through a one-way analysis of variance (SPSS 18.0, SPSS Inc., Chicago, USA), and significant differences within treatments ( $P < 0.05$ ) were evaluated using the Tukey's HSD multiple-range test.

## 3. Results And Discussion

### 3.1. Effect of ultrasonication on total protein extraction yield and solubility

The expression of specific energy released as a result of consumption of heat energy (produced from the conversion of dissipated power) by the sample matrix is correlated with factors such as medium viscosity, the mass of the sample, power input, exposure time, and temperature (Gonzalez-Centeno et al., 2014 and Strieder et al., 2019). The increased power and exposure duration of ultrasonic mediation promoted the maximum penetration of specific energy in 21.11–85.36 J mL<sup>-1</sup> range (Table S1). Figure 1A shows that a significant improvement in protein extraction after 5 min of ultrasonic treatment was feasible relative to the alkaline extracted samples, noted for each power input on this occasion. As expected, although the extraction yield was significantly increased from 5.76 to 83.61% with increasing power from 150 to 400 W, the trend of protein release was not linear along the processing time. At power level ranging between 250–350W, 20 min of sonication was adequate with no advantage to execute UAE beyond as the peak yield had been attained. As amplitude increases, ultrasonic shear waves distort and infiltrate the targeted cell walls constructively, leading to an improved mass movement ratio and facilitating the liberation of intracellular products into a solvent (Preece et al., 2017). In contrast, due to over-suspended impurities, extended sonication time might restrict solvent penetration into the cell walls. Nevertheless, when the sonication power extends to a higher time point beyond 20 min at 400 W, the yield declines considerably, probably due to the over-production of cavitation bubbles hindering the distribution of ultrasound waves. Following 20 min of treatment at 400 W, the highest protein yield was 36% greater than the yield obtained without sonication. Furthermore, protein solubility was found to increase gradually from 150 to 300 W along with time. However, after 15 min at 350 W and after 105 min at 400 W, the solubility seemed to decrease successively ( $p < 0.05$ ) (Fig. 1B).

For our subsequent studies, further analysis was carried out only with those samples having protein yield above 50%, produced upon UAE at 59.62 J mL<sup>-1</sup> (sample A), 64.13 J mL<sup>-1</sup> (sample B), 67.48 J mL<sup>-1</sup> (sample C), 63.23 J mL<sup>-1</sup> (sample D), 71.45 J mL<sup>-1</sup> (sample E) and 76.39 J mL<sup>-1</sup> (sample F).

### 3.2. Effect of ultrasonication on the particle size distribution

The particles in the solution before sonication ( $t = 0$ ) were in a highly aggregated and insoluble state, perhaps ascribed to the presence of fibers and chitin (found in Eri pupae as seen before in Longwah et al., 2011 study) within the aggregated structure. According to Fig. 2, the untreated sample primarily represented a trimodal dispersal of molecules in the entire size range between 0.5–2430  $\mu\text{m}$ . The peak in the scale of 0.5–2.3  $\mu\text{m}$  and 2.5–35  $\mu\text{m}$  might be due to some soluble and insoluble protein molecules distributed in the steady phase of the sample, respectively. In contrast, the larger-sized particles ( $> 35 \mu\text{m}$ ) were supposed to be related to the existence of intact cells, fibers, and chitin. A significant stepwise shift of the 2.5–35  $\mu\text{m}$  peak to a smaller range of 0.1–1.2  $\mu\text{m}$  was observed upon the rise in specific energy consumption from 59.6 to 64.1 J mL<sup>-1</sup>, which could be due to the reduction of insoluble protein particles into various size polymers or monomers which leads to improved solubilization. Particles within this diameter can be detected in the supernatant fraction after centrifugation. Such decrease in protein size in agglomerates must be credited to disturbances in intermolecular interactions, which generally support globular protein clusters in suspension, promoted by intense hydrodynamic micro-jets generated during acoustic cavitations. Deductions in protein sizes induced by ultrasound were widely documented for different systems (Jambrak et al., 2014; Preece et al., 2017). In contrast, the peak intensity of 0.1–1.2  $\mu\text{m}$  size range in sample C showed a minor shift, but these particle volumes were significantly reduced, followed by an increase in the formation of a peak at 2.5–37  $\mu\text{m}$  as well as volume in this case. While particles size distribution range extended to 3.9–95  $\mu\text{m}$  and 95–2430  $\mu\text{m}$  in sample E. Upon uptake of 76.4 J mL<sup>-1</sup> specific energy, particles aggregated extensively with broadening of distribution (bimodal pattern) peak, creating bigger particles of 2.0–1090  $\mu\text{m}$  sizes with the most significant fraction of  $>1 \mu\text{m}$  volume was 48.83%. Compared to the sample at  $t = 0$ , d [4,3] of  $<1 \mu\text{m}$  particles in ultrasound-treated samples shifted from 0.15  $\mu\text{m}$  to 0.20–0.25  $\mu\text{m}$  (Table S2).

### 3.3. Effect of ultrasonication on thermal characteristics

The gradual shifting of Eri pupae-derived proteins from their innate confirmation to a denatured position upon high-intensity UAE parameters can be recorded as varied endothermic changes (Table 1). Significant variations were noticed in the denaturation temperatures between alkaline extracted and ultrasound-assisted alkaline extracted EPPI. Compared to conventionally extracted proteins, those extracted upon consumption of specific energy 59.6 J mL<sup>-1</sup> showed no significant difference in denaturation temperature ( $T_d$ ). In contrast, samples B and C presented lower  $T_d$  values comparatively. Wherein, the enthalpy of denaturation ( $\Delta_H$ ) values consecutively reduced from 48.7 to 31.2 J g<sup>-1</sup> protein ( $P < 0.05$ ) for the protein isolates A–C, respectively, compared to control, suggesting some conformational transformation in these pupae proteins possibly due to the disruption or realignment of inter/intramolecular forces induced by strong cavitation waves at respective ultrasonic treatment. Sample D showed  $T_d$  and  $\Delta_H$  values having no significant difference with A and B, respectively. Due to minimal thermal stability, the lowest  $T_d$  and  $\Delta_H$  of 73.1°C and 31.2 J g<sup>-1</sup> were observed for sample C. However, higher energy consumption values at 71.4 and 76.4 J mL<sup>-1</sup> caused an appreciable increase in the  $T_d$  and  $\Delta_H$  values compared to those with the lowest values. Such enhancement might be attributed to the rearrangement of hydrophobic and disulfide bonds between unsettled protein conformations at secondary and tertiary levels (Chandrapala et al., 2012).

Table 1  
Thermal characteristics of Eri pupae proteins extracted with and without ultrasonic energy.

Thermal characteristics				
Samples	T <sub>o</sub> (° C)	T <sub>d</sub> (° C)	T <sub>e</sub> (° C)	Δ <sub>H</sub> (J/g)
Control	54.0 ± 0.2 <sup>a</sup>	94.2 ± 1.4 <sup>a</sup>	97.7 ± 0.5 <sup>e</sup>	48.7 ± 1.5 <sup>a</sup>
A	51.3 ± 1.2 <sup>b</sup>	90.5 ± 1.3 <sup>ab</sup>	112.4 ± 0.6 <sup>d</sup>	45.2 ± 1.6 <sup>b</sup>
B	47.5 ± 1.3 <sup>c</sup>	85.6 ± 1.2 <sup>c</sup>	122.3 ± 1.7 <sup>c</sup>	40.5 ± 1.3 <sup>c</sup>
C	46.1 ± 1.4 <sup>c</sup>	73.1 ± 1.4 <sup>e</sup>	128.2 ± 1.4 <sup>b</sup>	31.2 ± 0.5 <sup>e</sup>
D	46.3 ± 0.8 <sup>c</sup>	88.7 ± 1.3 <sup>b</sup>	128.3 ± 0.8 <sup>b</sup>	41.2 ± 1.5 <sup>c</sup>
E	42.1 ± 0.6 <sup>d</sup>	78.5 ± 1.3 <sup>d</sup>	133.5 ± 1.5 <sup>a</sup>	35.3 ± 0.8 <sup>d</sup>
F	37.7 ± 1.3 <sup>e</sup>	79.6 ± 1.3 <sup>d</sup>	135.5 ± 1.2 <sup>a</sup>	36.2 ± 0.7 <sup>d</sup>

Results are expressed as mean values ± standard deviations of n = 3. Different superscript letters in the same column represent statistical difference (p ≤ 0.05). T<sub>o</sub>: onset temperature, T<sub>d</sub>: denaturation temperature, T<sub>e</sub>: endset temperature, Δ<sub>H</sub>: enthalpy of denaturation.

### 3.4. Effect of ultrasonication on secondary structural characteristics as determined by FTIR spectroscopy

The stability of proteins released during sonication is essential to have a complete picture of how the proteins behave under ultrasound conditions concerning their conformational and physicochemical changes. Therefore, in this study, the extracted protein's conformational characteristics were detected in the amide I spectral location between 1700 and 1600 cm<sup>-1</sup>, representing the C = O expanding resonance of the peptide bonds. The collected spectrum of extracted pupae protein samples distinctly demonstrated the result of ultrasonic energy in differential peak intensities followed by a secondary structure pattern noted for α-helix (1651-53 cm<sup>-1</sup>), intermolecular and intramolecular β-sheets (1620 and 1632 cm<sup>-1</sup>), aggregated β-sheets (1700 – 1694 cm<sup>-1</sup>), β-turns (1667-84 cm<sup>-1</sup>), 3<sub>10</sub>-helices (1661-64 cm<sup>-1</sup>), and random unordered structures (1644-48 cm<sup>-1</sup>) (Grewal et al., 2017).

The obtained spectra were derivatized (mentioned in section 2.6.) to distinctly isolate the overlapping bands so that subsequent alterations due to individual treatments could be anticipated (Fig. 3A and B), which were not deducible with the native protein spectra.

Table 2 summarizes the overall percentage areas of various secondary conformations belonging to the amide I region in pupae proteins as a function of specific treatment integration. Table 3 compiled the band intensity (percentage) of particular constituents of β-sheet and β-turn conformations. As represented in both **Tables (2 and 3)**, the peak intensity for α-helix was slightly reduced (p < 0.05) for sample B, and there was a considerable reduction in β-sheet component at 1619 and 1630 cm<sup>-1</sup> followed by considerable elevation in β-sheet peak intensity at 1640 and 1634 cm<sup>-1</sup>. While no such significant variation for α-helix intensity was observed for samples A and D, the β-sheet intensity peak at 1628 and 1640 cm<sup>-1</sup> increased remarkably. Instead of rearrangement patterns in different β-sheet components, no significant alteration in the overall β-sheet peak area was noted for samples A, B, and D compared to control.

Table 2  
Total percentage areas of secondary conformations in amide I region of FTIR spectra.

Conformational element	Wavenumber (cm <sup>-1</sup> )	Area (%)							SE <sup>a</sup>
		Control	A	B	C	D	E	F	
α-helix	1651-53	13.6 <sup>e</sup>	13.2 <sup>e</sup>	10.5 <sup>d</sup>	9.3 <sup>c</sup>	13.4 <sup>e</sup>	1.3 <sup>a</sup>	6.3 <sup>b</sup>	0.4
Total β-sheet	1619-42, 1688-97	48.4 <sup>a</sup>	50.3 <sup>a</sup>	48.0 <sup>a</sup>	52.5 <sup>b</sup>	49.8 <sup>a</sup>	58.2 <sup>c</sup>	57.1 <sup>c</sup>	1.3
Total β-turn	1667-84	16.4 <sup>a</sup>	17.2 <sup>a</sup>	16.3 <sup>a</sup>	16.0 <sup>a</sup>	15.8 <sup>a</sup>	16.5 <sup>a</sup>	26.7 <sup>b</sup>	0.4
Large loops	1656-58	3.5 <sup>b</sup>	3.4 <sup>b</sup>	3.1 <sup>b</sup>	3.1 <sup>b</sup>	3.3 <sup>b</sup>	2.1 <sup>a</sup>	4.1 <sup>b</sup>	0.4
Random	1644-48	2.7 <sup>a</sup>	2.3 <sup>a</sup>	2.8 <sup>a</sup>	2.8 <sup>a</sup>	2.6 <sup>a</sup>	4.6 <sup>b</sup>	4.6 <sup>b</sup>	0.4
3 <sub>10</sub> -helices	1661-64	7.3 <sup>b</sup>	6.7 <sup>b</sup>	7.4 <sup>b</sup>	9.4 <sup>c</sup>	6.6 <sup>b</sup>	3.8 <sup>a</sup>	5.9 <sup>b</sup>	0.7

Means in the same row that do not share the same letters differ significantly (p ≤ 0.05).

<sup>a</sup> Standard error for all summed up data for a particular secondary structure.

Table 3  
Percentage areas of  $\beta$ -sheet and  $\beta$ -turn obtained from amide I region in FTIR spectra.

Band assignment	Control		A		B		C		D		E		F
	Band frequency (cm <sup>-1</sup> )	Area (%)	Band frequency (cm <sup>-1</sup> )	Area (%)	Band frequency (cm <sup>-1</sup> )	Area (%)	Band frequency (cm <sup>-1</sup> )	Area (%)	Band frequency (cm <sup>-1</sup> )	Area (%)	Band frequency (cm <sup>-1</sup> )	Area (%)	Band frequency (cm <sup>-1</sup> )
$\beta$ -sheet	1619	3.0 <sup>b</sup>	1619-20	3.2 <sup>b</sup>	1619	2.2 <sup>a</sup>	1620	5.8 <sup>c</sup>	1619	3.0 <sup>b</sup>	1620	7.7 <sup>d</sup>	1620
$\beta$ -sheet	1624	7.1 <sup>c</sup>	1623-25	6.6 <sup>c</sup>	1623	7.3 <sup>c</sup>	1623-24	3.3 <sup>a</sup>	1624	6.8 <sup>c</sup>	1624	4.1 <sup>b</sup>	1624
$\beta$ -sheet	1629-30	11.4 <sup>c</sup>	1628	13.3 <sup>d</sup>	1630	8.7 <sup>a</sup>	1630	10.8 <sup>b</sup>	1628	12.9 <sup>d</sup>	1630	15.7 <sup>e</sup>	1630
$\beta$ -sheet	1632-34	9.5 <sup>b</sup>	1633-34	8.8 <sup>b</sup>	1634	11.4 <sup>c</sup>	1633	13.8 <sup>d</sup>	1633	9.1 <sup>b</sup>	1632	11.3 <sup>c</sup>	1632
$\beta$ -sheet	1640	10.0 <sup>b</sup>	1640	12.5 <sup>c</sup>	1640	11.6 <sup>c</sup>	1639	10.6 <sup>b</sup>	1640	13.0 <sup>d</sup>	1640	8.8 <sup>a</sup>	1640
$\beta$ -sheet	1689	5.2 <sup>a</sup>	1688-89	4.4 <sup>a</sup>	1688	5.2 <sup>a</sup>	1690	5.5 <sup>a</sup>	1688	4.6 <sup>a</sup>	1689	5.4 <sup>a</sup>	1688
$\beta$ -sheet	1700 – 1694	2.4 <sup>a</sup>	1693-94	1.8 <sup>a</sup>	1692-93	2.1 <sup>a</sup>	1695	2.7 <sup>a</sup>	1692	2.0 <sup>a</sup>	1694,1698	5.2 <sup>b</sup>	1694
$\beta$ -turn	1669	4.8 <sup>a</sup>	1668	4.5 <sup>a</sup>	1668	4.7 <sup>a</sup>	1669	4.4 <sup>a</sup>	1669	5.0 <sup>a</sup>	1667-69	6.3 <sup>b</sup>	1669
$\beta$ -turn	1674	3.0 <sup>a</sup>	1674	3.3 <sup>a</sup>	1672-73	2.8 <sup>a</sup>	1674	2.4 <sup>a</sup>	1673	3.2 <sup>a</sup>	1674	2.9 <sup>a</sup>	1673-74
$\beta$ -turn	1679	6.5 <sup>b</sup>	1678-79	6.2 <sup>b</sup>	1678-79	6.2 <sup>b</sup>	1678	7.2 <sup>b</sup>	1678	6.4 <sup>b</sup>	1679	3.7 <sup>a</sup>	1678-79
$\beta$ -turn	1683	2.1 <sup>a</sup>	1682-83	1.8 <sup>a</sup>	1682	2.3 <sup>a</sup>	1683	1.6 <sup>a</sup>	1683	2.0 <sup>a</sup>	1683	3.6 <sup>b</sup>	1683
Means in the same row that do not share the same letters differ significantly ( $p \leq 0.05$ ).													
<sup>a</sup> Standard error for all summed up data for a particular secondary structure.													

Moreover, other secondary conformations did not seem to be significantly influenced by the sonication process for samples A, B, and D. In contrast with the control sample, samples C, E, and F exhibited maximum structural changes with an increase in varied disorganized structure induced by ultrasound extraction. Thus, when sonication power increased from 300 to 400 W and increasing time, the  $\alpha$ -helix peak intensity declined to 9.3% at the ultrasonic energy value of 67.5 J mL<sup>-1</sup>. This peak nearly diminished at 71.4 J mL<sup>-1</sup>; however, it reappeared at 76.4 J mL<sup>-1</sup> (Table 2). For sample C (at 76°C), total  $\beta$ -sheet (Table 1) rise by 4.1%, with a significant decline in the intensity of the band allotted to  $\beta$ -sheets at 1623-24 cm<sup>-1</sup> accompanied by a significant enhancement in  $\beta$ -sheet component at 1620 and 1633 cm<sup>-1</sup> and  $3_{10}$  helices (1663 cm<sup>-1</sup>) (Table 3).

The spectra obtained for samples E and F indicated that these conditions influenced the secondary conformation of proteins broadly in contrast with other samples. Intense variations were observed for sample E (at 83°C) with enhancement in the intensity of  $\beta$ -sheet constituent (particularly at 1630 cm<sup>-1</sup>, 1694 cm<sup>-1</sup> and 1698 cm<sup>-1</sup>) and intermolecular  $\beta$ -sheets (1620 cm<sup>-1</sup>) at the cost of  $\beta$ -sheet constituent (1624 cm<sup>-1</sup>) ( $P < 0.05$ ). PCA analysis further confirmed these data by separating samples according to sonication treatment along PC1 and PC2, elucidating 92 and 5% of deviation, respectively (Fig. 4A and B). PCA separated control from selected ultrasound extracted samples followed by grouping into samples A, B, and D; sample C; samples E, and F, inferring considerable alterations in the protein secondary conformation in each group. Sample E was distinguished from the remaining samples towards PC1 with maximum loading for 1620–1640 cm<sup>-1</sup> implying considerable structural reorganization of  $\beta$ -sheets at the evaluated temperature, accompanied by decreased ( $P < 0.05$ ) loops (1657 cm<sup>-1</sup>; 2.1%) and  $3_{10}$ -helix (1661–1663 cm<sup>-1</sup>, 3.8%) along with the slightly increased formation of turns (at 1667–1669 cm<sup>-1</sup>; 6.3% and 1683 cm<sup>-1</sup>; 3.6%), reduced  $\beta$ -turn at 1679 cm<sup>-1</sup> (with no significant change in total  $\beta$ -turn intensity %) and increased random structures (at 1645–1647 cm<sup>-1</sup>, 4.6%) (Tables 2 and 3), suggesting various proportions of sub-agglomerates development due to protein denaturation. Compared to control, prolonged treatment at 76.39 J mL<sup>-1</sup> (97°C) exhibited  $\beta$ -sheet element at 1632 cm<sup>-1</sup> correlated to intramolecular sheet components to reduce from 9.5–4.6% as well as a  $\beta$ -sheet element at 1620 and 1694 cm<sup>-1</sup> correlated to intermolecular sheet components and its aggregates to increase by 7.2% and 6.3% (Table 3), respectively, accompanied by significant improvement in  $\beta$ -turns (peak 1673–1674 cm<sup>-1</sup>, 1678–1679 cm<sup>-1</sup>) by 10.3% and random conformation (1646–1648 cm<sup>-1</sup>) by 2%. The loading plot further confirmed the observations, which indicated that sample F was isolated through PC2 with reduced loading in the zone 1629–1640 cm<sup>-1</sup> and profound loading in peak region 1694–1700 cm<sup>-1</sup> assigned to aggregates. It also presented a maximum loading for  $\alpha$ -helix, substantiating the previous finding of recurrence of this conformation. Thus, the temperature factor was more evident when it inclined above 75°C, causing major shifts in the 1620–1642 cm<sup>-1</sup> range, particularly with a deviation of intermolecular  $\beta$ -sheets.

### 3.5. Effect of ultrasonication on structural characteristics as determined by Raman spectroscopy

UAE caused appreciable alterations in Raman spectra (400–3000 cm<sup>-1</sup>) of proteins framework (Fig. 5), specific assignments, and percentage area of individual bands in amide I and III regions after curve-fitting analysis (Fig. 6) are outlined in Table 4. Compared to control, which had the highest  $\alpha$ -helix content of 82.3%, enhancement in ultrasonic energy produced upon extension in sonication power and treatment duration instigated a drift towards helix uncoiling, which was established by the reduction (of peak intensity centered at 1322 and 1647 cm<sup>-1</sup> (contributing to  $\alpha$ -helix) accompanied by increased

intensity of peak at  $1243\text{ cm}^{-1}$  and  $1668\text{--}1675\text{ cm}^{-1}$  allotted to  $\beta$ -sheet. Especially when the ultrasonic energy was between  $63.2\text{ J mL}^{-1}$  and  $71.4\text{ J mL}^{-1}$ , the evident band intensity near  $1668\text{--}1675\text{ cm}^{-1}$  became significantly dominant in sample E, indicating the gradual formation of sheets. However, this elevation in  $\beta$ -sheet absorbance was not somehow detected in the Raman spectrum obtained from sample C (in contrast to what we have found in FTIR spectra), probably because particles present might jumble and developed protein matrix rapidly, resulting in a rapid change to measure. However, minor variations existed within UAE samples. For example, it was noticed that the absorption peak at  $1647\text{ cm}^{-1}$  was significantly broadened by 6% in sample F, highlighting the remodeling of the protein's secondary constitution. In addition, two peaks appeared at  $1664$  and  $1670\text{ cm}^{-1}$  (depicting random coil) in sample E, which successively became broader in sample F. Such observation is consistent with FTIR data which is sufficient enough to explain the transition of Raman bands analysis as sonication proceeded.

Table 4  
Total percentage areas of Raman peaks.

Conformational element	Band frequency ( $\text{cm}^{-1}$ )	Area (%)							SE <sup>a</sup>
		Control	A	B	C	D	E	F	
$\alpha$ -helix	1322	36.0 <sup>e</sup>	33.4 <sup>d</sup>	34.2 <sup>d</sup>	31.4 <sup>c</sup>	33.8 <sup>d</sup>	24.3 <sup>b</sup>	16.2 <sup>a</sup>	1.4
$\alpha$ -helix	1647	46.3 <sup>c</sup>	44.4 <sup>c</sup>	45.8 <sup>c</sup>	40.5 <sup>b</sup>	45.2 <sup>c</sup>	32.5 <sup>a</sup>	52.4 <sup>d</sup>	1.0
$\beta$ -sheet	1243	7.3 <sup>a</sup>	7.1 <sup>a</sup>	6.7 <sup>a</sup>	6.8 <sup>a</sup>	7.0 <sup>a</sup>	12.5 <sup>b</sup>	14.5 <sup>c</sup>	0.6
$\beta$ -sheet	1668-75	5.4 <sup>a</sup>	6.2 <sup>a</sup>	4.9 <sup>a</sup>	4.1 <sup>a</sup>	5.2 <sup>a</sup>	9.7 <sup>b</sup>	12.1 <sup>c</sup>	0.7
Random coil	1664	0.5 <sup>b</sup>	0.4 <sup>b</sup>	0.6 <sup>b</sup>	0.3 <sup>a</sup>	0.6 <sup>b</sup>	3.7 <sup>c</sup>	6.3 <sup>d</sup>	1.2
Random coil	1670	0.7 <sup>a</sup>	0.8 <sup>a</sup>	0.6 <sup>a</sup>	0.8 <sup>a</sup>	0.7 <sup>a</sup>	3.4 <sup>b</sup>	5.7 <sup>c</sup>	1.1
C-H stretching vibrations	2929	10.5 <sup>a</sup>	24.8 <sup>e</sup>	26.6 <sup>f</sup>	31.4 <sup>g</sup>	18.4 <sup>d</sup>	12.8 <sup>b</sup>	20.2 <sup>c</sup>	0.4
C-H stretching vibrations	1448-50	8.2 <sup>a</sup>	9.1 <sup>a</sup>	8.5 <sup>a</sup>	18.5 <sup>d</sup>	7.4 <sup>a</sup>	12.3 <sup>b</sup>	15.6 <sup>c</sup>	
CH <sub>2</sub> , CH <sub>3</sub> stretching vibrations	1440-65	7.3 <sup>a</sup>	8.5 <sup>a</sup>	7.9 <sup>a</sup>	27.5 <sup>d</sup>	8.1 <sup>a</sup>	16.3 <sup>b</sup>	19.2 <sup>c</sup>	0.7
Tryptophan	760	5.7 <sup>a</sup>	4.2 <sup>a</sup>	5.1 <sup>a</sup>	14.7 <sup>c</sup>	6.2 <sup>a</sup>	16.1 <sup>c</sup>	10.8 <sup>b</sup>	0.5
Tyrosine	$\nu_{850/830}$	0.6 <sup>a</sup>	1.3 <sup>c</sup>	2.1 <sup>d</sup>	3.2 <sup>e</sup>	2.5 <sup>d</sup>	3.2 <sup>e</sup>	0.8 <sup>b</sup>	0.7
Means in the same row that do not share the same letters differ significantly ( $p \leq 0.05$ ).									
<sup>a</sup> Standard error for all summed up data for a particular secondary structure.									

To identify the pattern of disulfide bonds, the wavelength region within  $500\text{--}550\text{ cm}^{-1}$  assigned to the S-S bridge was evaluated because it was noticed that peak intensity between  $2570\text{--}2575\text{ cm}^{-1}$  assigned to  $\text{--SH}$  stretching vibration was eventually decreased, illustrating transformation into S-S bond (Fig. 5). However, an observed shift and changes in Raman peaks and bands intensities, respectively, which suggests alterations in S-S bridge conformation and content (Fig. 7i) have also occurred. Based on Fig. 7 presenting the outcome of deconvoluted spectra (Fig. 7(ii-viii)) of S-S bonds illustrating for control and sample A-F, it was noticed that for samples B and D, the relative content of  $\text{S-S}_{(t-g-g)}$  ( $522\text{ cm}^{-1}$ ) depicting trans-gauche-gauche conformation was significantly reduced due to breakage of S-S bond (Fig. 7ix). In contrast, no considerable variation existed for the remaining band's intensity. This result contrasts with the sample without sonication, where the corresponding intensity of  $510$  and  $522\text{ cm}^{-1}$  peaks were considerably high, and the peak at  $545\text{ cm}^{-1}$  was comparably low. For sample C, the relative intensity of  $\text{S-S}_{(g-g-g)}$  at  $510\text{ cm}^{-1}$  depicting gauche-gauche-gauche conformation shifted to  $515\text{ cm}^{-1}$  and gradually reduced; the relative intensity of  $\text{S-S}_{(t-g-g)}$  conformation steadily increased to 34% and shifted from  $520$  to  $527\text{ cm}^{-1}$ , no significant change was noted for  $\text{S-S}_{(t-g-t)}$  ( $545\text{ cm}^{-1}$ ) content depicting trans-gauche-trans conformation (Fig. 7ix). It indicates gradual unfolding of the  $\alpha$ -helix and rearrangement into other conformations, which caused alteration of C-C and C-S bond brought by S-S stretching vibration with a considerable rise in temperature as reported by Wu et al. (2019). As ultrasonic energy continues to rise above  $70\text{ J mL}^{-1}$ , the content of  $\text{S-S}_{(t-g-t)}$  was increased to  $49.3 \pm 2.2\%$  (sample E) and  $59.1 \pm 1.6\%$  (sample F) with consecutive blue shift and reduction in  $\text{S-S}_{(g-g-g)}$  as well as  $\text{S-S}_{(t-g-g)}$  content as compared to the one obtained without treatment (Fig. 7 ix), leading to new unstable intermolecular S-S bond formation (Xiong et al., 2020). Therefore, this could contribute to the rapid aggregation of subunits.

Raman spectroscopy was more sensitive to polar, non-polar, and aliphatic stretching vibrations, whereas these bands were difficult to detect and isolate in FTIR spectroscopy (Sun et al., 2011). Therefore, according to Kobayashi et al. (2017), Raman spectra could be utilized to estimate protein's hydrophobic core surroundings and, thus, an essential feature adding to the texture, tenderness, and shear force of the sample. The Raman peak spotted near  $2929\text{ cm}^{-1}$  is generally credited to the C-H elasticity. The elevated intensity of this peak is brought by an exhibition of protein's hydrophobic aliphatic amino acid side chains. In our study, the peak intensity at  $2929\text{ cm}^{-1}$  successively decreased from sample  $\text{C} > \text{B} > \text{A} > \text{D} > \text{F} > \text{E}$  (Table 4). The lowest intensity of this band in sample E is because ultrasound-induced denaturation of pupae proteins (as seen in their secondary structural FTIR data) might have aided the proteins to aggregates, resulting in less exposure. However, an extension of ultrasonic energy input possibly caused these aggregates to get slightly loosened due to increased heating since denaturation followed by helix refolding was observed in the above section, thus resulting in slightly higher band intensity in sample F. In contrast to these results, no significant difference in the intensity of the peak at  $1448\text{--}50\text{ cm}^{-1}$  was observed among sample A, B, and D compared to alkaline

extracted protein. Sun et al. (2011) reported that Raman bands closer to  $1440\text{--}1465\text{ cm}^{-1}$  were contributed by  $\text{CH}_2$ ,  $\text{CH}_3$  bending vibrations. Similarly, in agreement with what we have seen for peaks at  $2929\text{ cm}^{-1}$ , this band intensity pattern was also highest in sonicated sample C due to maximum aliphatic side chain exposure causing increased hydrophobic interactions between the residues and then significantly declining upon extraction at 400 W between 15 to 20 min, indicating the cross-linking possibly due to formation of gelation in sample E and F (Table 4). This data is consistent with the tryptophan absorption peak at  $760\text{ cm}^{-1}$  (Table 4) which explains the polarity of the microenvironment nearby hydrogen bonds. While in the present study, as expected with gradual increase of temperature as an outcome of increased ultrasonic energy,  $I_{850/830}$  also consecutively increased to  $\geq 1.3$  (for samples A, B, and D), suggesting exposure of tyrosine residues on the protein surface (Table 4). Particularly, with the rise in temperature above  $70^\circ\text{C}$  due to input of ultrasonic energy more than  $\sim 65\text{ J mL}^{-1}$ , the  $I_{850/830}$  can reach nearly 3.2 (samples C and E), indicating intense hydrogen bond receiving behavior of tyrosine residues as a result of exposure in the polar microenvironment. However, sample F showed a lower value of  $I_{850/830}$  (0.8) because of the involvement of tyrosine residues to interact intermolecularly in their refolded and buried position (Zhang et al., 2015). Also, the peaks at 2014, 2168, and  $2420\text{ cm}^{-1}$  gradually disappeared with an increase in ultrasonic energy input, which probably depicts the development of firm 3-D network-like structures (Fig. 5). It suggested that different shear constraints developed due to variation in cavitation environment could temper or modify the shape of Eri pupae protein released in the solvent in different ways.

### 3.5. Effect of ultrasonication on structural characteristics as determined by intrinsic fluorescence

The primary fundamental fluorescence emissions from tryptophan residues additionally impart a sensitive mode of identifying protein conformations by providing details regarding the regional environment of tryptophan which comprises nearby amino acids and background hydrophobicity (Christensen et al., 2006). Figure 8A shows an overlaid plot of the averaged and area normalized emission spectra for tryptophan ( $F_{\text{Trp}}$ ) in samples A-F. The Trp residues present in the control sample exhibited two emission spectra at 341.7 and 355 nm on account of the two adjacent isoenergetic transition positions. For samples A and B, the emission spectra' essence and intensity remain unimpaired ( $p > 0.05$ ) perhaps due to more negligible structural alteration. In contrast, sample C showed increased emission intensity by 6.8%, which peaks at around 345 nm denoting protein structural reorganization leading to some denatured pupae protein assemblies with a group of Trp residues bonded; possibly due to the physiochemical medium generated during the given sonication condition. Sample C also displayed a significant red shift to 365 nm besides improving emission strength. Such distinguished spectrum shifts specify exposure of Trp residues located in the released pupae proteins to the solvent during sonication due to conformational changes in protein unfolding, aggregation, and oligomerization (Lakowicz, 2006). Sample D also exhibited a slight elevation in emission peak compared to control, but the change was appeared to be non-significant. On the other hand, Trp fluorescence intensity peak in samples E and F decreased by 6.5 and 8.5% with increased sonication power and treatment time. Due to the rise in shear waves and resulting thermal activities during sonication, Trp emission got highly quenched due to the bonding of Trp components with nearby amino acid moieties suggesting a conformational reorganization of the protein entities (as seen in FTIR data). Moreover, the emission intensity values suggested that the quenching is relatively more substantial in sample F compared to E, which perhaps indicates that the extent of structural modification is higher in sample F compared to E, which could be because of a further increase in cavitation intensity accompanied by an increase in a temperature to  $95^\circ\text{C}$ . In addition, the structured emission spectra for sample F disappeared. In contrast, they persisted to a specific extent for sample E, highlighting that the Trp moieties in sample F encounter a homogeneous molecular domain. The surroundings of the Trp residues possibly got slightly more hydrophobic in this case since, compared to sample C, there was less and no clear red shift observed in the emission maxima for samples E and F, respectively, suggesting that the Trp moieties in the protein complexes were not exposed the way sample C did. Such difference in hydration ability promotes Trp moieties of proteins present in sample C to remain in its more humid phase than the Trp moieties of proteins in samples E and F with a less hydrated core. Such variation in the position and content of denatured protein corresponded to the heterogeneous and aggregated behavior (obtained in confocal microscopy; Fig. 9) in samples E and F compared to the homogeneous microstructure of the control sample. Hence, the Trp moieties encounter a vital domain in the entire sonication process.

In addition, since dityrosine is a molecular marker of protein oxidation, the formation of the dityrosine bonds might provide knowledge regarding protein complexes and their globular structure (Scheidegger et al., 2013). Therefore, during sonication, the cavitation stress and temperature elevation would promote the likelihood and energy for tyrosine residues to unmask and connect, which will aid in the increase in  $F_{\text{dt}}$  intensity, found to be highest in sample E, followed by samples C and F (Fig. 8B). The metal ion's existence, matrix complexity, and protein structure are the principal factors determining the coverage of dityrosine appearance in proteins (Liu et al., 2018; Scheidegger et al., 2013).

Overall, these results explained variation in particle size and thermal analysis data observed within the samples and agree with the study done by Li and Xiong (2021). They previously described the thermal effect produced during the sonication process in developing protein-protein clusters.

### 3.3. The proteome of Eripupae

To further understand the nature of individual proteins in Eri pupae, we performed proteomic analysis of the proteins extracted in sample D (with high protein yield and minimal structural distortion) in our subsequent study.

SDS-PAGE evaluation of supernatant and pellet fragments procured from ultrasound ( $63.23\text{ J mL}^{-1}$ ) assisted complete protein yield from Eri pupae inferred the existence of diverse proteins (Fig. 10A and 10B). Under the reduced state, supernatant revealed that the molecular weight (mol. wt) of proteins ranged from  $\sim 10$  to 245 kDa, though proteins within  $\sim 16$  to 33 kDa range were typical (28.7%) (Lane1, Fig. 10A). Notably, in supernatant fraction, the molecular masses pattern of Eri pupae proteins seemed slightly inconsistent under non-reduced and reduced conditions (Lane 1, Fig. 10B). This differentiation possibly highlights several perspectives, comprising multimeric noncovalent oligomers, protein-protein assembly, or collective subunits that might play an efficient role in silkworm pupae metabolic management. Likewise, investigation of pellets presented in reduced (Lane 2, Fig. 10A) and non-reduced (Lane 2, Fig. 10B) state demonstrates the presence of molecules with molecular masses ranging from  $\sim 15$  to 33 kDa. Meanwhile, it was observed that  $\sim 15\text{--}19\text{ kDa}$  weight proteins were prevalent (16.2%) in pellet parts in both states based on a densitometry survey. Moreover, the intensity percentage of bands present in gel sections 1 (Mol

wt > 45 kDa), 2 (Mol wt 20–45 kDa), 3 (Mol wt 16–20 kDa), and 4 (Mol wt 10–15 kDa) in the supernatant and also for gel sections 1 (Mol wt > 23 kDa) and 2 (Mol wt 10–23 kDa) corresponding to pellet fraction were convincingly consistent with the relative availability of Eri pupae proteins, inferred by LC-MS/MS examination (Fig. 10C and Fig. 11).

The abundance of proteins presents in supernatant and pellet as deduced by mass spectrometry evaluation agreed with the corresponding ions in Eri pupae (Table S3). The matrix-assisted laser desorption/ionization-time of flight-mass spectrometry evaluation of supernatant and pellet fractions suggested the existence of overall 80 and 38 discrete ions within m/z scale of 5.4 to 247 kDa and 5.5 to 50 kDa, respectively (Table S3). Although unavailability of a substantial corresponding database makes this procedure of quantifying pupae protein limits our study. At the same time, the present study's data agrees with the corresponding band intensities depicting diverse Eri pupae proteins.

MS/MS-attained peptide's amino acid order aligned with the matched databank proteins is presented in Fig. S1. 107 distinct proteins in Eri pupae assigned to 26 insect protein families were deduced via MS/MS investigation of trypsin cleaved total 4 and 2 gel segments of pellet and supernatant (Table S4, Table S5). Eighty-two enzymatic and non-enzymatic molecules assigned to 22 discrete insecta protein families (see Table S4) were established in the supernatant fraction. In contrast, 25 enzymatic and non-enzymatic molecules assigned to 8 discrete insecta protein families were spotted (see Table S4) in the pellet. The comparative availability of diverse groups of proteins presents in Eri pupae as established by the proteomic investigation is shown in Fig. 11 in detail. Thus, it was demonstrated that the Eri pupae proteome was prevailed by a non-enzymatic section of proteins that accounted for 60% of the proteome closely.

## 4. Conclusion

The data procured in this study has not only provided an initial understanding of how pupae proteins constituents reorganize under a sonic induced cavitation environment, potentially leading to physical changes, but also verified the suitability of combined vibrational and fluorescence spectroscopy for rapidly predicting ultrasonic energy stability of EPPI during ultrasound-assisted extraction through in-line surveillance. Additionally, the information on individual proteins available in Eri pupae could improve the predictive ability to identify the protein-protein interactions responsible for the functional characteristics of any future product developed with EPPI.

## Declarations

### Acknowledgements

Authors are thankful to Sankur Phukan (Department of Chemical Science, Tezpur University, India), Dipankar Kalita (Department of FET, Tezpur University, India), Arup Jyoti Das (Department of FET, Tezpur University, India), Manoj Sharma (Department of MBBT, Tezpur University, India) and Mass spectrometry team (RGCB, Kerala, India and SAIF, IIT Bombay).

### Declaration of competing interest

The authors have no competing interests to declare that are relevant to the content of this article.

### Funding source

This research did not receive any specific grant from funding agencies in the public, commercial, or not-for-profit sectors.

## References

1. Akande, A.O., Jolayemi, O.S., Adelugba, V.A., & Akande, S.T. (2020). Silkworm pupae (*Bombyx mori*) and locusts as alternative protein sources for high-energy biscuits. *Journal of Asia-Pacific Entomology*, *23*, 234-241. <https://doi.org/10.1016/j.aspen.2020.01.003>.
2. Bao, C., Liu, B., Li, B., Chai, J., Zhang, L., Jiao, L., Li, D., Yu, Z., Ren, F., Shi, X., & Li, Y. (2020). Enhanced transport of shape and rigidity-tuned  $\alpha$ -Lactalbumin nanotubes across intestinal mucus and cellular barriers. *Nano Letters*, *20*, 1352-1361. <https://doi.org/10.1021/acs.nanolett.9b04841>.
3. Chandrapala, J., Zisu, B., Kentish, S., & Ashokkumar, M. (2012). The effects of high-intensity ultrasound on the structural and functional properties of  $\alpha$ -Lactalbumin,  $\beta$ -Lactoglobulin and their mixtures. *Food Research International*, *48*, 940-943. <https://doi.org/10.1016/j.foodres.2012.02.021>.
4. Christensen, J., Nørgaard, L., Bro, R., & Engelsen, S. B. (2006). Multivariate autofluorescence of intact food systems. *Chemical Reviews*, *106*, 1979-1994. <https://doi.org/10.1021/cr050019q>.
5. David-Birman, T., Romano, A., Aga, A., Pascoviche, D., Davidovich-Pinhas, M., & Lesmes, U. (2021). Impact of silkworm pupae (*Bombyx mori*) powder on cream foaming, ice cream properties and palatability. *Innovative Food Science & Emerging Technologies*, *75*, 102874. <https://doi.org/10.1016/j.ifset.2021.102874>.
6. Feyzi, S., Milani, E., & Golimovahhed, Q.A. (2018). Grass pea (*Lathyrus sativus* L.) protein isolate: the effect of extraction optimization and drying methods on the structure and functional properties. *Food Hydrocolloids*, *74*, 187-196. <https://doi.org/10.1016/j.foodhyd.2017.07.031>.
7. Gonzalez-Centeno, M.R., Knoerzer, K., Sabarez, H., Simal, S., Rossello, C., & Femenia, A. (2014). Effect of acoustic frequency and power density on the aqueous ultrasonic-assisted extraction of grape pomace (*Vitis vinifera* L.)—a response surface approach. *Ultrasonics Sonochemistry*, *21*, 2176-2184. <https://doi.org/10.1016/j.ultsonch.2014.01.021>.
8. Grewal, M. K., Chandrapala, J., Donkor, O., Apostolopoulos, V., & Vasiljevic, T. (2017). Predicting sediment formation in ultra-high temperature-treated whole and skim milk using attenuated total reflectance-Fourier transform infrared spectroscopy. *International Dairy Journal*, *74*, 39-48. <https://doi.org/10.1016/j.idairyj.2017.01.004>.

9. Jambrak, A. R., Mason, T. J., Lelas, V., Paniwnyk, L., & Herceg, Z. (2014). Effect of ultrasound treatment on particle size and molecular weight of whey proteins. *Journal of Food Engineering*, *121*, 15-23. <https://doi.org/10.1016/j.jfoodeng.2013.08.012>.
10. Kadam, S. U., Tiwari, B. K., Álvarez, C., & O'Donnell, C. P. (2015). Ultrasound applications for the extraction, identification and delivery of food proteins and bioactive peptides. *Trends in Food Science & Technology*, *46*, 60-67. <https://doi.org/10.1016/j.tifs.2015.07.012>.
11. Kang, D., Zhang, W., Lorenzo, J. M., & Chen, X. (2021). Structural and functional modification of food proteins by high power ultrasound and its application in meat processing. *Critical Reviews in Food Science and Nutrition*, *61*, 1914-1933. <https://doi.org/10.1080/10408398.2020.1767538>.
12. Kim, H. W., Setyabrata, D., Lee, Y. J., Jones, O. G., & Kim, Y. H. B. (2016). Pre-treated mealworm larvae and silkworm pupae as a novel protein ingredient in emulsion sausages. *Innovative Food Science & Emerging Technologies*, *38*, 116-123. <https://doi.org/10.1016/j.ifset.2016.09.023>.
13. Kobayashi, Y., Mayer, S. G., & Park, J. W. (2017). FT-IR and Raman spectroscopies determine structural changes of tilapia fish protein isolate and surimi under different comminution conditions. *Food Chemistry*, *226*, 156-164. <https://doi.org/10.1016/j.foodchem.2017.01.068>.
14. Lakowicz, J. R. (Ed.). (2006). *Principles of fluorescence spectroscopy*. Boston, MA: Springer US.
15. Li, R., & Xiong, Y. L. (2021). Ultrasound-induced structural modification and thermal properties of oat protein. *LWT*, *149*, 111861. <https://doi.org/10.1016/j.lwt.2021.111861>.
16. Liu, J., Zamora, A., Castillo, M., & Saldo, J. (2018). Modeling of the changes in bovine milk caused by ultra-high pressure homogenization using front-face fluorescence spectroscopy. *Journal of Food Engineering*, *233*, 88-97. <https://doi.org/10.1016/j.jfoodeng.2018.04.010>.
17. Longvah, T., Mangthya, K., & Ramulu, P. (2011). Nutrient composition and protein quality evaluation of eri silkworm (*Samia ricinii*) prepupae and pupae. *Food Chemistry*, *128*, 400-403. <https://doi.org/10.1016/j.foodchem.2011.03.041>.
18. Luna, G.C., Martin-Gonzalez, F.S., Mauer, L.J., & Liceaga, A.M. (2021). Cricket (*Acheta domesticus*) protein hydrolysates' impact on the physicochemical, structural and sensory properties of tortillas and tortilla chips. *Journal of Insects as Food and Feed*, *7*, 109-120. <https://doi.org/10.3920/JIFF2020.0010>.
19. Mishra, N., Hazarika, N.C., Narain, K., & Mahanta, J. (2003). Nutritive value of non-mulberry and mulberry silkworm pupae and consumption pattern in Assam, India. *Nutrition Research*, *23*, 1303-1311. [https://doi.org/10.1016/S0271-5317\(03\)00132-5](https://doi.org/10.1016/S0271-5317(03)00132-5).
20. Preece, K. E., Hooshyar, N., Krijgsman, A., Fryer, P. J., & Zuidam, N. J. (2017). Intensified soy protein extraction by ultrasound. *Chemical Engineering and Processing: Process Intensification*, *113*, 94-101. <https://doi.org/10.1016/j.cep.2016.09.003>.
21. Sarkar, P., Valacchi, G., & Duary, R. K. (2022). Proteome composition and profiling of bioactive peptides of edible *Antheraea assamensis* pupae by sequential enzymatic digestion and kinetic modeling of in vitro gastrointestinal digestion. *European Food Research and Technology*, *248*, 357-379. <https://doi.org/10.1007/s00217-021-03882-z>.
22. Scheidegger, D., Radici, P.M., Vergara-Roig, V.A., Bosio, N.S., Pesce, S.F., Pecora, R.P., Romano, J.C.P., & Kivatinitz, S.C. (2013). Evaluation of milk powder quality by protein oxidative modifications. *Journal of Dairy Science*, *96*, 3414-23. <https://doi.org/10.3168/jds.2012-5774>.
23. Shirsath, S. R., Sonawane, S. H., & Gogate, P. R. (2012). Intensification of extraction of natural products using ultrasonic irradiations—A review of current status. *Chemical Engineering and Processing: Process Intensification*, *53*, 10-23. <https://doi.org/10.1016/j.cep.2012.01.003>.
24. Strieder, M. M., Silva, E. K., & Meireles, M. A. A. (2019). Specific energy: a new approach to ultrasound-assisted extraction of natural colorants. *probe*, *23*, 30. <https://doi.org/10.5923/j.fph.20190902.02>.
25. Sun, W., Zhao, Q., Zhao, M., Yang, B., Cui, C., & Ren, J. (2011). Structural evaluation of myofibrillar proteins during processing of Cantonese sausage by Raman spectroscopy. *Journal of Agricultural and Food Chemistry*, *59*, 11070-11077. <https://doi.org/10.1021/jf202560s>.
26. Tellez-Morales, J. A., Hernandez-Santo, B., & Rodriguez-Miranda, J. (2020). Effect of ultrasound on the techno-functional properties of food components/ingredients: A review. *Ultrasonics Sonochemistry*, *61*, 104787. <https://doi.org/10.1016/j.ultsonch.2019.104787>.
27. Wu, M., Cao, Y., Lei, S., Liu, Y., Wang, J., Hu, J., Li, Z., Liu, R., Ge, Q., & Yu, H. (2019). Protein structure and sulfhydryl group changes affected by protein gel properties: process of thermal-induced gel formation of myofibrillar protein. *International Journal of Food Properties*, *22*, 1834-1847. <https://doi.org/10.1080/10942912.2019.1656231>.
28. Xiong, L., Boeren, S., Vervoort, J., & Hettinga, K. (2021). Effect of milk serum proteins on aggregation, bacteriostatic activity and digestion of lactoferrin after heat treatment. *Food Chemistry*, *337*, 127973. <https://doi.org/10.1016/j.foodchem.2020.127973>.
29. Zhang, Z., Yang, Y., Tang, X., Chen, Y., & You, Y. (2015). Chemical forces and water holding capacity study of heat-induced myofibrillar protein gel as affected by high pressure. *Food Chemistry*, *188*, 111-118. <https://doi.org/10.1016/j.foodchem.2015.04.129>.
30. Zhao, X., Vázquez-Gutiérrez, J. L., Johansson, D. P., Landberg, R., & Langton, M. (2016). Yellow mealworm protein for food purposes-extraction and functional properties. *PLoS One*, *11*, e0147791. <https://doi.org/10.1371/journal.pone.0147791>.
31. Zhou, Z.F., Ren, Z.X., Yu, H.Y., Jia, J.Q., & Gui, Z.Z. (2017). Effects of different modification techniques on molecular structure and bioactivity of *Bombyx mori* pupa protein. *Journal of Asia-Pacific Entomology*, *20*, 35-41. <https://doi.org/10.1016/j.aspen.2016.11.008>.
32. Zielinska, E., Baraniak, B., Karas, M., Rybczynska, K., & Jakubczyk, A. (2015). Selected species of edible insects as a source of nutrient composition. *Food Research International*, *77*, 460-466. <https://doi.org/10.1016/j.foodres.2015.09.008>.

## Figures

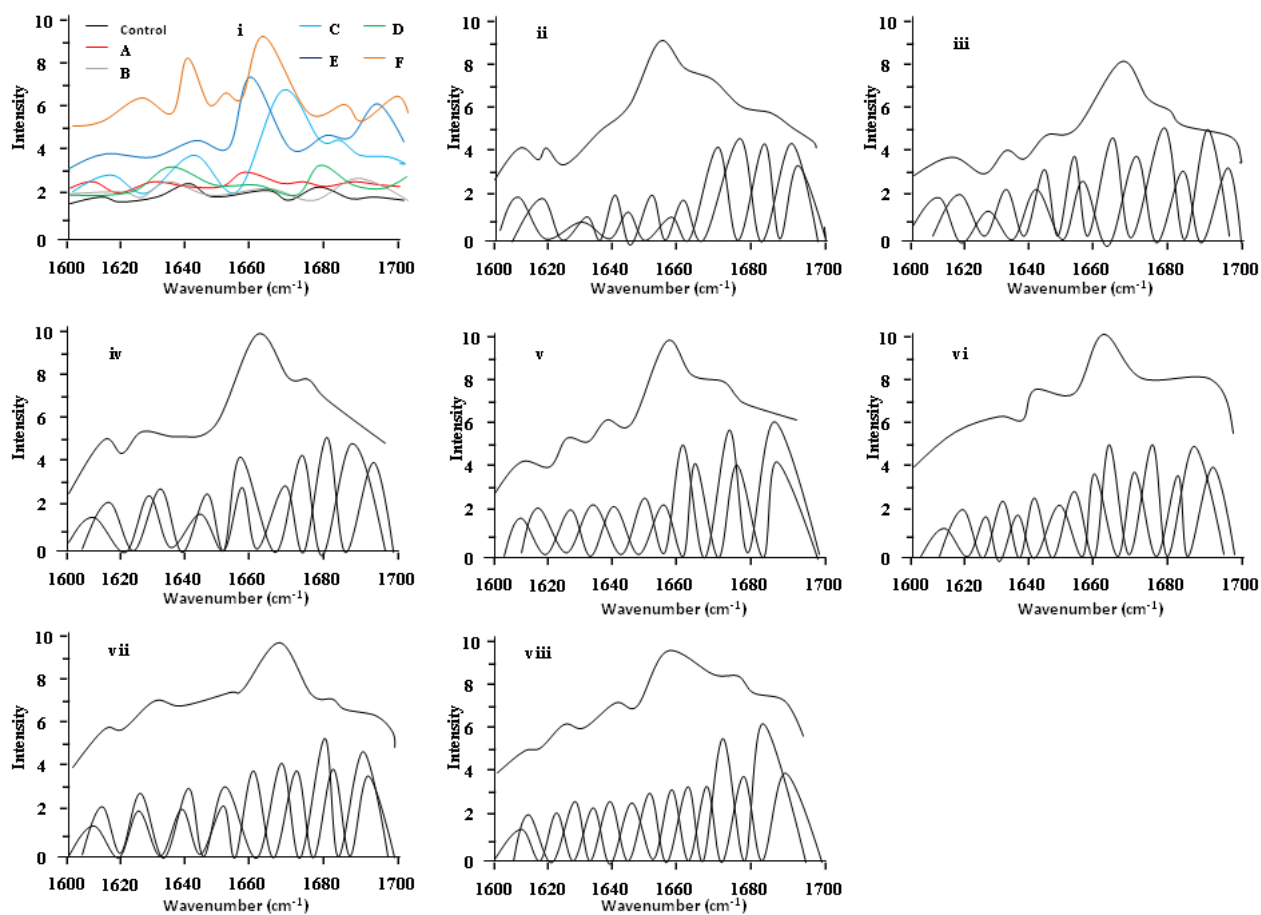


Figure 6

Raman spectra of (i) amide I and amide III regions, (ii) Control, (iii) Sample A, (iv) Sample B, (v) Sample C, (vi) Sample D, (vii) Sample E and (viii) Sample F.

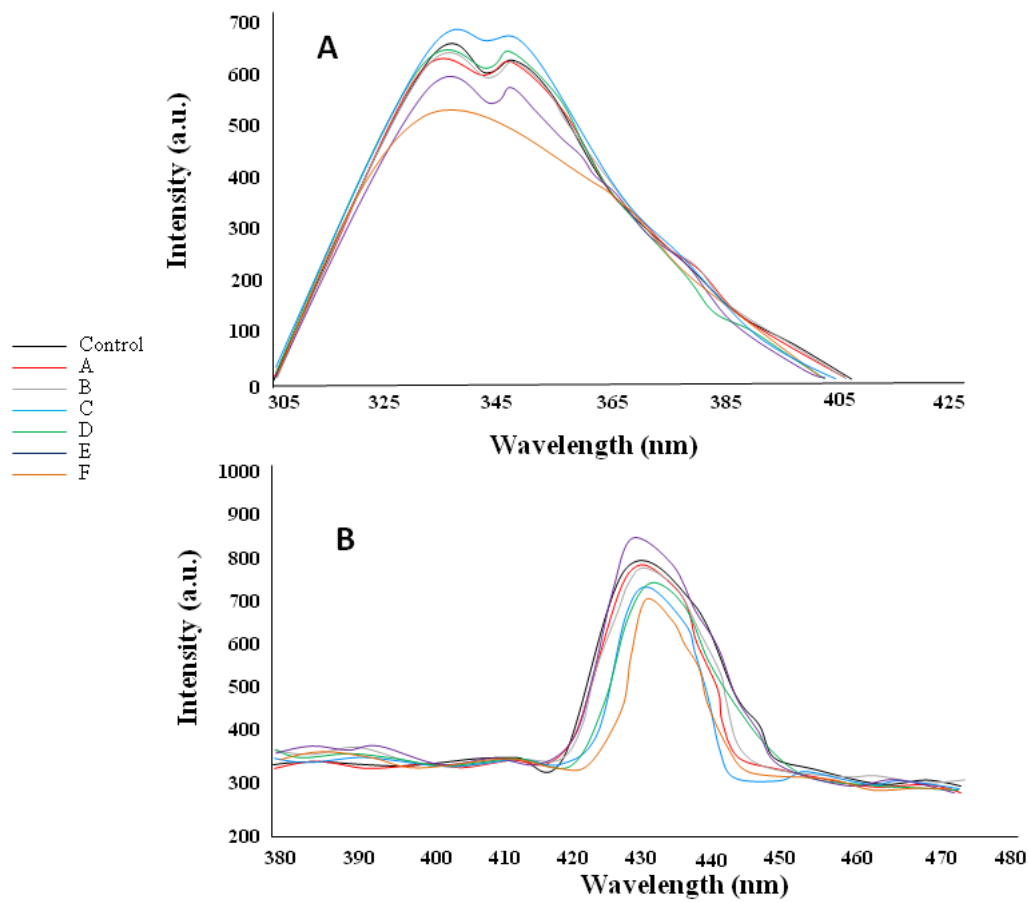


Figure 8

Fluorescence spectra of (A) tryptophan emission intensity at 290 nm and (B) dityrosine tryptophan emission intensity at 315 nm.

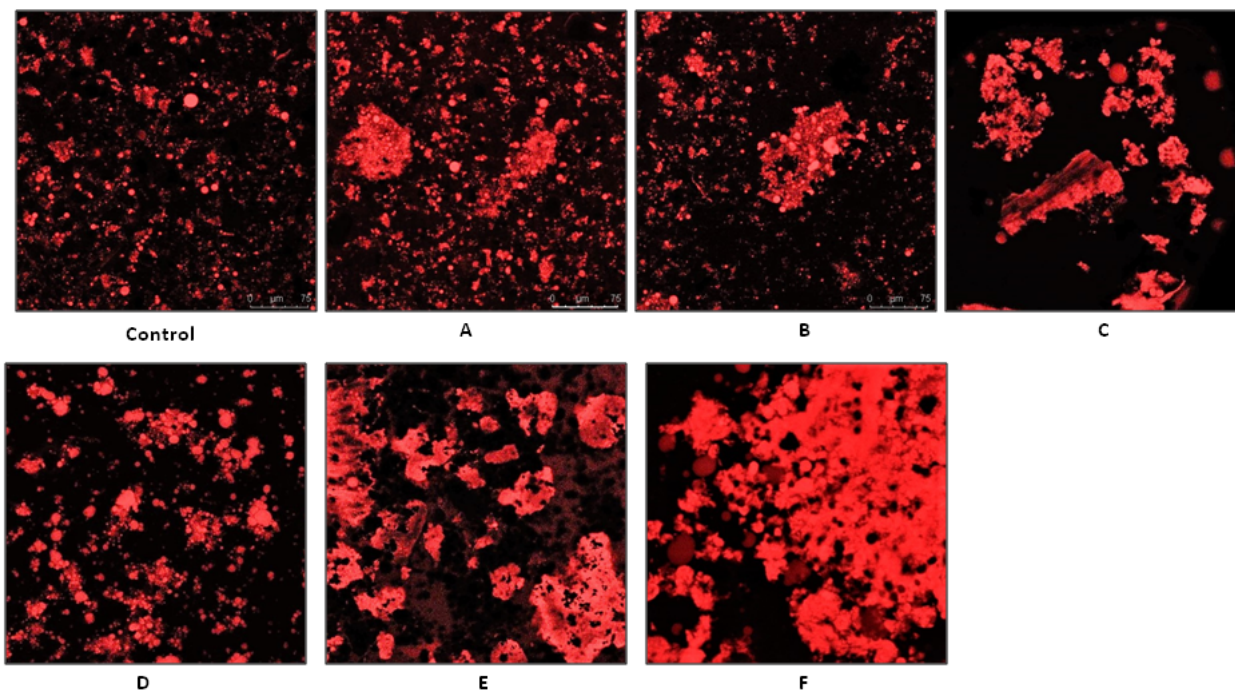
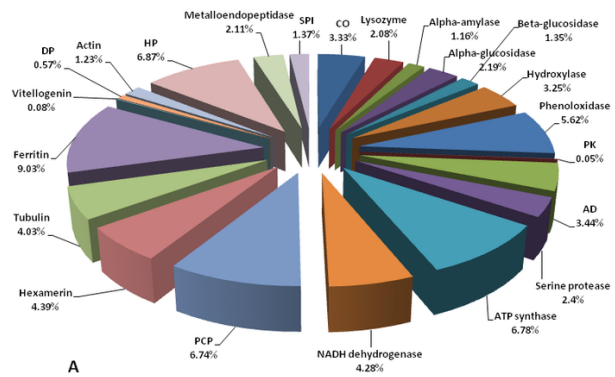
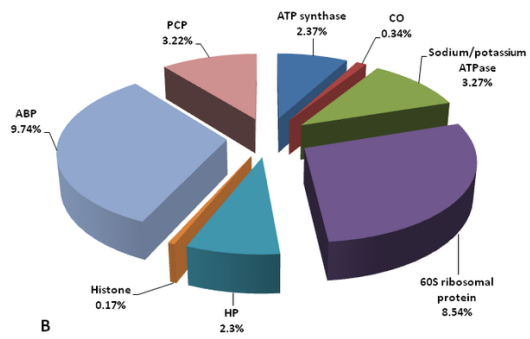


Figure 9

Confocal scanning microscopic images of control, (A) Sample A, (B) Sample B, (C) Sample C, (D) Sample D, (E) Sample E and (F) Sample F



A



B

**Figure 11**

Protein family constitution of EPPi. Pie chart illustrates the relative existence of various enzymatic and non-enzymatic protein families of Eri pupae in (A) Supernatant and (B) Pellet sections. Individual protein descriptions are illustrated in Figure S1 and Table S3 and S4.